Materialia 23 (2022) 101462

Contents lists available at ScienceDirect

Materialia

journal homepage: www.elsevier.com/locate/mtla

Full Length Article

Validation of a capillary-driven fragmentation model during mixed columnar-equiaxed solidification with melt convection and grain transport

Christian M.G. Rodrigues[a], Menghuai Wu[a,*], Haijie Zhang[a], Andreas Ludwig[a], Abdellah Kharicha[a,b]

[a] Metallurgy Department, Chair of Simulation and Modeling Metallurgical Processes, Montanuniversitaet of Leoben, Franz-Josef Street 18, Leoben 8700, Austria
[b] Christian-Doppler Laboratory for Metallurgical Application of Magnetohydrodynamics, Montanuniversitaet of Leoben, Franz-Josef Street 18, Leoben 8700, Austria

ARTICLE INFO

Keywords:
Fragmentation
Model validation
Microstructural transition
Alloy solidification
Volume-average model
Remelting

ABSTRACT

A mixed columnar-equiaxed solidification model was recently extended to capture the capillary-driven fragmentation phenomenon, which was considered the only mechanism for the formation of equiaxed crystals. The purpose of the present study was to validate the model by replicating a laboratory experiment on the solidification of an aqueous ammonium chloride solution (Gao and Wang, 1999). The experiment was performed by cooling the solution in a vertical test cell from the top surface to allow columnar dendrites to grow. Owing to the fragmentation of the downward-growing columnar dendrites, equiaxed fragments appeared, sedimented, and created a bed of crystals at the bottom of the cell. This pile-up of crystals ultimately met the columnar-tip front coming from the top, thereby leading to a structural transition (columnar-to-equiaxed transition). This experiment was successfully reproduced numerically for the first time, which involved coupling between the following phenomena: fragmentation, melt convection, grain transport, a pile-up of equiaxed crystals, and the potential growth of columnar dendrites from a bed of equiaxed crystals (equiaxed-to-columnar transition). A satisfactory agreement was achieved between the simulation and experimental results. Knowledge about capillary-driven fragmentation was strengthened by analyzing the microstructural evolution. Alloy-dependent parameters S_{s0}, K_0, and a that govern dendrite coarsening and fragmentation were proposed for an aqueous ammonium chloride solution. Finally, the limitations of the current version of the fragmentation model were discussed.

1. Introduction

A comprehensive simulation of the structural evolution of industrial-based castings is beyond the scope of existing numerical models owing to an intricate coupling between all physical phenomena involved in the solidification process. For instance, in laboratory-controlled experiments conducted by Gao and Wang [1], solidification kinetics, fragmentation, melt flow, crystal transport, crystal pile-up, and columnar-to-equiaxed transition (CET) were some of the phenomena observed. However, in practical applications, the physics involved may be even more complex.

Equiaxed crystals in metal-alloy castings can originate from heterogeneous nucleation or crystal fragmentation. The former can be achieved by adding grain refiners to the melt shortly before casting; the latter arises from the remelting of the roots of high-order dendrite arms of the columnar structure during coarsening [2]. Fragmentation is a potent intrinsic grain-refinement mechanism that can promote CET [3].

Fragmentation is an important phenomenon that has been widely studied [4–6]. A recent microgravity experiment aboard the International Space Station [7] revealed that the fragmentation rate, $\dot{N}_{\mathrm{V}}$, can be expressed in terms of the characteristic length scale of the dendrites in a mush as follows:

$$\dot{N}_{\mathrm{V}} \equiv \frac{\mathrm{d}N_{\mathrm{V}}}{\mathrm{d}t} = \frac{\mathrm{d}\left(a \cdot \left(\frac{S_{\mathrm{V}}}{f_{\mathrm{s}}}\right)^{3}\right)}{\mathrm{d}t} \tag{1}$$

where a is an alloy-dependent constant equal to 0.5×10^{-4} for a Pb-Sn alloy; f_{s} is the volume fraction of the solid; and S_{V} is the interfacial area density. For the entire casting spectrum, S_{V} can be calculated as follows [8]:

$$S_{\mathrm{V}} = f_{\mathrm{s}}(1 - f_{\mathrm{s}})^{\mathrm{r}}\left(\left(S_{\mathrm{s0}}{}^{-1}\right)^{3} + K_{0}t_{\mathrm{s}}\right)^{-1/3} \tag{2}$$

where r, S_{s0}, and K_0 are alloy-dependent fitting constants, and t_{s} (local solidification time) is the time from the first appearance of a local columnar structure.

---

[*] Corresponding author.
E-mail address: menghuai.wu@unileoben.ac.at (M. Wu).

https://doi.org/10.1016/j.mtla.2022.101462
Received 1 March 2022; Accepted 24 May 2022
Available online 26 May 2022
2589-1529/© 2022 The Author(s). Published by Elsevier B.V. on behalf of Acta Materialia Inc. This is an open access article under the CC BY license (http://creativecommons.org/licenses/by/4.0/)

Melt convection plays a critical role in the entire process of fragmentation by transporting the fragments out of the mushy zone [9] and increasing the fragmentation potential [10,11] owing to flow-induced variations in temperature and/or solute enrichment [12]. The melt temperature also influences the evolution of the fragments ahead of the columnar front. Under superheating conditions, remelting of the fragments can occur, which shortens their lifetimes [3]. Strong flows have been found to increase the probability of fragment survival [13] because they increase the likelihood of the fragments to reach potential supercooled melt regions away from the fragmentation events.

Although the physics underlying the fragmentation mechanism is relatively well understood, very few computational models have been able to couple the major solidification-accompanying phenomena with fragmentation. For instance, Neumann-Heyme et al. [14] performed 3D phase-field simulations to capture the dynamics of the detachment of a single dendritic-side branch from the main stem. The focus was on the evolution of the interfacial area of the dendrites; however, the flow effect was ignored. Wesner et al. [15] evaluated the influence of processing conditions on dendrite fragmentation using phase-field simulations. Contrary to the study by Neumann-Heyme et al. [14], the dendritic structure was cooled and the relationship between temperature and fragmentation dynamics was analyzed. Zhang et al. [16] analyzed the microstructural evolution of dendrite coarsening using a quantitative cellular automaton model. The model consisted of a simplified version of the thermodynamics and kinetics of solidification and the numerical results were validated using analytical predictions. However, coarsening dynamics have only been studied during isothermal holding. More recently, Zheng et al. [17] designed a practical model to replicate the fragmentation phenomenon in casting processes based on the local remelting theory by Flemings [18]. According to this theory, a flow parallel to the columnar-growth direction promotes remelting in the mushy zone that presumably triggers fragmentation. This practical model did not rely on the capillary-driven fragmentation theory; thus, non-isothermal conditions and the melt flow in the columnar-growth direction were required.

This study is a follow-up to a recent publication by the present authors [19] where capillary-driven fragmentation was implemented in a mixed columnar-equiaxed volume-average solidification model. The effects of the multiphase transport phenomena on the outcome were also analyzed. Some parameters of the model were verified against the results available in the literature. However, the fragmentation implementation was not fully validated against objective experimental data. This was addressed in the present work. Gao and Wang [1] conducted experiments to investigate the effect of fragmentation on the CET in an aqueous ammonium chloride solution. The experimental conditions were varied systematically. Corresponding quantitative data were provided for each case, as well as some shadowgraphs. Here, we used our model to reproduce these experiments, evaluate the results, and explore the limitations of the model.

2. Model description

2.1. Mixed columnar-equiaxed solidification model

The three-phase volume-average model for mixed columnar-equiaxed solidification has been described elsewhere [20,21]. A general outline of the proposed model is presented in this section.

The three phases are liquid, solid columnar, and solid equiaxed, and the sum of their volume fractions (f_ℓ, f_c, and f_e) is unity. For diffusion-governed solidification kinetics, the columnar dendrites were simplified as cylinders growing unidirectionally along the temperature gradient. The position of the columnar-primary-dendrite tip was tracked by considering the dendrite-growth kinetics according to the Lipton–Glicksman–Kurz model [22]. The equiaxed grains were assumed to be spherical. The growth of the equiaxed phase was governed by solute diffusion in the interdendritic melt and the concentration difference ($c_\ell{}^* - c_\ell$) acted as the driving force for solidification. Thermodynamic equilibrium was assumed at the solid-liquid interface, which determined the species concentration $c_\ell{}^*$ at this location. The back diffusion in the solid and solidification shrinkage were neglected.

To address the hydrodynamic interaction between the phases, equiaxed crystals were represented as grain envelopes that included solid dendrites and interdendritic melts. The ratio of the volume of the solid dendrites to that of the equiaxed-grain envelope, f_si, was set to a constant value of 0.16. The volume fraction of the grain envelopes, $f_\mathrm{e}{}^\mathrm{env}$, was represented by the following relationship: $f_\mathrm{e}{}^\mathrm{env} = f_\mathrm{e} \,/\, f_\mathrm{si}$. When $f_\mathrm{e}{}^\mathrm{env}$ surpassed the packing limit, $f_\mathrm{e,packing}$, of 0.637, the equiaxed phase became a rigid body. The momentum-conservation equations were solved for the equiaxed and liquid phases, whereas the columnar phase was assumed to be rigid and stationary. The species and enthalpy conservation equations were solved for all three phases, and an additional transport equation for the equiaxed phase was solved to account for the evolution of the number of grains created by fragmentation. The thermosolutal convection of the melt and crystal sedimentation were modeled using the Boussinesq approximation. Heterogeneous nucleation was neglected, which assumed that equiaxed crystals can only originate from fragmentation. A linearized binary phase diagram was used with a constant solute redistribution coefficient, k, and liquidus slope, m.

Under superheating conditions, the remelting of the equiaxed grains was considered. The remelting process included two steps: reduction in the grain size, and destruction of the grain. The reduction of the grain size was modeled according to the diffusion-governed kinetics, and the driving force was the constitutional superheating: when the concentration difference ($c_\ell{}^* - c_\ell$) was negative, remelting occurred. Once the grain became smaller than a minimum critical diameter (set to 30 μm), the grain was eliminated from the domain. The remelting model was described in detail in [23].

2.2. Fragmentation model

Details of the fragmentation model have been previously reported [19]. The fragmentation model comprises four main equations (Table 1). $\dot{N}_\mathrm{V}$ is the frequency at which the fragments detached from the columnar structure. This was calculated using the time derivative of the product of a and the cube of S_V [7]. S_V was determined by the coarsening law (Eq. (2)) and comprises the interfacial evolution during the solidification-dominant stage (1st term in the equation) and coarsening-dominant stage (2nd term in the equation).

Referring to Fig. 1, a large S_V implies that the columnar structure has grown numerous high-order arms. Based on Eq. (3), a large S_V also indicates that the potential for fragmentation increases owing to the low energy requirements needed to remelt the roots of the smaller high-order dendrite arms. Following this understanding, the sizes of the detached fragments are assumed to decrease with the increase in S_V, according to Eq. (5). The corresponding mass of each created fragment is transferred from the columnar phase to the equiaxed phase. This is captured by Eq. (4).

2.3. Experiment and model configuration

In [1], experiments were conducted to systematically investigate the fragmentation and effect of the fragment (grain) transport on the CET. A transparent aqueous ammonium chloride solution (NH_4Cl-H_20) was

Table 1

Main equations of the fragmentation model.

Interfacial area density	$S_\mathrm{V} = f_\mathrm{c}(1 - f_\mathrm{c})^\mathrm{r}\left(\left(S_\mathrm{s0}{}^{-1}\right)^3 + K_0 t_\mathrm{s}\right)^{-1/3}$	(2)
Fragmentation rate	$\dot{N}_\mathrm{V} = \frac{\mathrm{d}(a \cdot S_\mathrm{V}{}^3)}{\mathrm{d}t}$	(3)
Columnar-to-equiaxed mass transfer	$M_\mathrm{ce} = \dot{N}_\mathrm{V}\left(\rho_\mathrm{e} \frac{\pi}{6}\left(d^0_\mathrm{frag}\right)^3\right)$	(4)
Size of the created fragments	$d^0_\mathrm{frag} = f_\mathrm{c} \frac{1.6}{S_\mathrm{V}}$	(5)

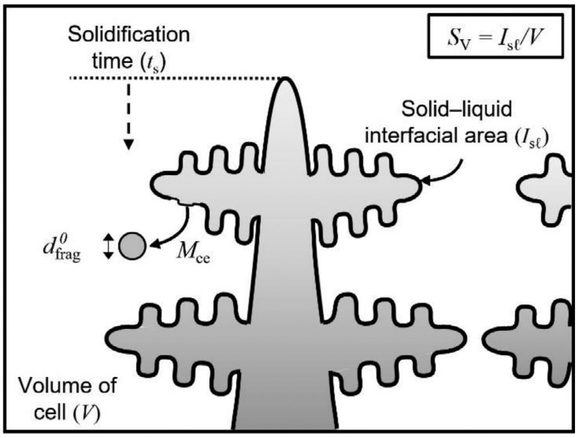

Fig. 1. Schematic diagram of the fragmentation process and the parameters of interest.

used, and the experiments were performed in a vertical test cell (dimensions 4.2 × 2.8 × 1.27 cm^3) that was cooled from the top. Removable covers were used on the front and back walls for optical access to the interior. The remaining walls were isolated. Six thermocouples were mounted on the side panel of the test cell to monitor the temperature. The probe tips were positioned in the midplane. A shadowgraph visualization system and a normal camera were used to capture the images of the solidification front, flow structures, and bed of fragments. Fig. 2(a) shows a schematic of the test cell and specifies the relative positions of the probes.

Five experiments were conducted at various temperatures of the cold-top surface, $T^{0,\text{top}}$, the initial temperature of the melt, T^0, and the initial concentration of the alloy, c_0. The results are summarized in Table 2. Depending on the test case, the melt began at different levels of superheating ranging from 1 K (test cases 1 and 2) to 13 K (test case 4). Additionally, the nominal composition of the model alloy varied from 68.0 wt.% to 66.0 wt.% H_2O in test case 2, and the cold plate temperature changed from 254.15 K to 259.15 K in test case 5.

The key phenomena observed in the experiments are summarized as follows. Fragmentation occurred after the formation of the columnar dendrites on the top wall. The created fragments were assumed to be the only source of the equiaxed crystals, i.e., the formation of the equiaxed crystals by heterogeneous nucleation was negligible. The fragments sedimented because they were heavier than the liquid. Some of these survived the superheat in the bulk-melt region and piled up at the bottom of the cell, thereby creating a bed of fragments. Finally, the continuous growth of the equiaxed-sediment bed resulted in a CET when the interface of the bed contacted the columnar-tip front coming from the top.

For the simulations, a similar test-cell configuration was adopted, as shown in Fig. 2(b). The 3D domains were divided into 3×10^4 cells. The flow boundary conditions were no-slip for the liquid and solid phases. Adiabatic boundary conditions were used for the insulated walls. A convective heat transfer boundary condition for the front and back wall with a small heat transfer coefficient (HTC) (20 W/(m^{2}K)) and room temperature (T_∞ = 300 K) were used to replicate the periodic optical access required during the experiments. A convective heat transfer boundary condition for the top surface with a large HTC (2000 W/(m^{2}K)) was used to replicate the imposed intense-cooling conditions. For numerical reasons, the initial equiaxed-solid fraction $f_e{}^0$ was set to a negligible value (1×10^{-5}). The complete list of the material properties for the model alloy (NH_4Cl-H_20) is presented in Table 3. Although NH_4Cl-H_20 has been extensively studied, the fragmentation parameters, K_0, S_{s0}, and a (Eqs. (2) and (3)), of the model alloys are still unknown. These parameters were deduced in the subsequent section based on the results presented in [1].

Table 2
Initial conditions for the five test cases.

Test case	c_0 [wt.% H_20]	T^0 [K]	$T^{0,\text{top}}$ [K]	T_{liquidus} [K]
1	68.0	316.15	254.15	315.15
2	66.0	325.48	254.15	324.48
3	68.0	320.15	254.15	315.15
4	68.0	328.15	254.15	315.15
5	68.0	320.15	259.15	315.15

3. Simulation results

3.1. Solidification sequence

The solidification sequence at t = 10 s, t = 100 s, t = 500 s, and t = 1000s for test case 1 is shown in Fig. 3. To interpret the results, a schematic representation of the main mechanisms during the sequence is shown in Fig. 3(a). The growth of the columnar dendrites, fragmentation events, grain transport, and growth of the bed of fragments (pile-up) are depicted in the figure. Fig. 3(b)–(e) represent the corresponding simulation results for f_c, N_v, f_e, and c_ℓ (liquid solute concentration), respectively. The f_c and f_e contours are overlaid with $\vec{u}_\ell$ and $\vec{u}_e$ vectors, respectively. The c_ℓ contour is overlaid with temperature (T) isolines. A quarter of the domain on the right was removed for the visualization of the internal fields. The following fragmentation parameters were assumed in the simulations: a = 100, $(S_{s0})^{-1}$ = 100 μm, and K_0 = 2350 μm^3/s. This selection was explained later in a subsequent section.

At t = 10 s (Fig. 3(a1))–(e1)), a columnar structure developed from the top surface (f_c, Fig. 3(b1)) owing to the cooling of this surface (T isolines in Fig. 3(e1)). With the local solidification at the top, the melt became enriched in solute c_ℓ (Fig. 3(e1)). Fragments also appeared in the columnar-mushy zone near the top of the cell (N_v, Fig. 3(c1)) as the source of equiaxed crystals. Because the fragments were heavier than the melt, they started to sediment (downward $\vec{u}_e$ arrows in Fig. 3(d1)), but they did not reach the bottom surface. As a result, melt was forced to travel upward ($\vec{u}_\ell$arrows in Fig. 3(b1)) to give space for the sinking grains. Notably, when interacting with the first fragments, the melt flow was disturbed and created a local counter-clockwise motion in the center of the domain.

At t = 100 s (Fig. 3(a2)–(e2)), a pile-up of the fragments was observed at the bottom surface (f_e, Fig. 3(d2)). This means that the first fragments already reached the bottom surface and the temperature in the bulk melt is below T_{liquidus} (isolines in Fig. 3(e2)). At the same time, more fragments were created (N_v, Fig. 3(c2)) and sedimented ($\vec{u}_e$ arrows in Fig. 3(d2)). At this particular moment, besides the upward melt flow closer the wall, another strong upward melt flow appeared in the center of the domain ($\vec{u}_\ell$arrows in Fig. 3(b2)). The central upward flow was due to the circumstantial low f_e values found in the center of the domain in the earlier stages of the simulation, which reduced the drag in that region and facilitated the local melt flow. A unidirectional temperature field continued to develop downward (isolines in Fig. 3(e2)), which extended the columnar mushy zone (f_c, Fig. 3(b2)) as well as the region of potential fragmentation (N_v, Fig. 3(c2)). Also, in Fig. 3(c2), N_v increased towards the top surface because t_s increased towards the roots of the dendrites, which increased S_V and $\dot{N}_V$ locally (see Eqs. (2) and (3)).

As the solidification progressed, the fragmentation rate decreased, which slowed down the pile-up of the bed of fragments. Note that a columnar structure can develop from the packed equiaxed bed if it is locally undercooled and no sufficient equiaxed fragments continue to pile up. This phenomenon, also referred to as an equiaxed-to-columnar transition (ECT) event, can be observed at t = 500 s where the columnar structure (f_c, Fig. 3(b)) started to grow faster than the existing bed of fragments (f_e, Fig. 3(d3)). This is particularly evident closer to the front

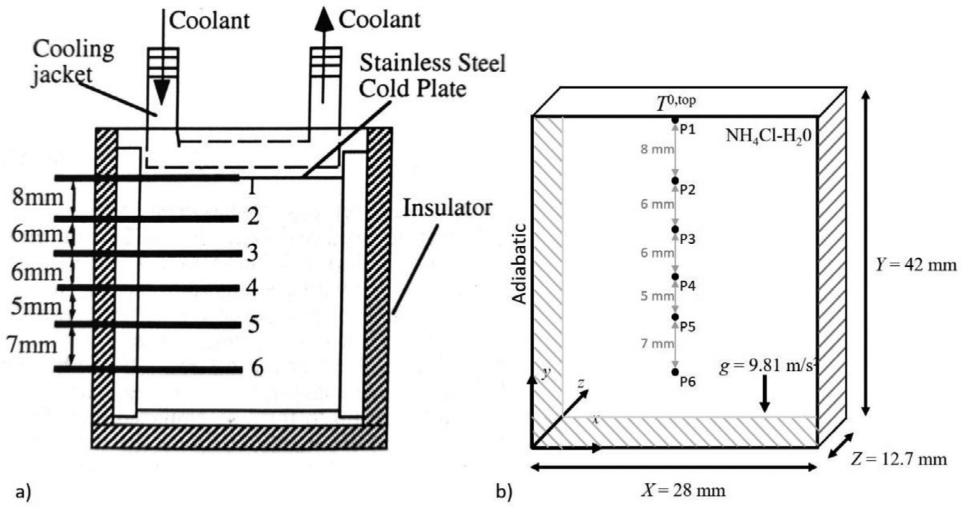

Fig. 2. (a) Schematic of the test cell (image replicated from [24] - Copyright © 1998 by The Minerals, Metals & Materials Society. Used with permission.) and (b) the geometry and boundary conditions for the simulations.

Table 3
Material properties and parameters.

	Symbol	Units	NH_4Cl-H_20	Sources
Thermodynamic properties (local linearized phase diagram)				
Nominal composition	c_0	wt.% H_20	varied according to the experiment (Table 2)	[1]
Liquidus temperature	T_{liquidus}	K	varied with composition (Table 2)	[1]
Melting point of the solvent at $c_0 = 0$	T_f	K	638.15	extrapolation
Eutectic composition	c_{eut}	wt.%	80.3	[1]
Eutectic temperature	T_{eut}	K	257.75	[1]
Liquidus slope	M	K (wt.%)$^{-1}$	−4.75	[25]
Partition coefficient	K	–	0	[25]
Gibbs–Thomson coefficient	Γ	m•K	4.0×10^{-8}	[26]
Thermo-physical properties				
Reference density	ρ_ℓ, ρ_s	kg•m^{-3}	1073.0	[27]
Specific heat	$c_p{}^\ell$, $c_p{}^s$	J•kg^{-1}•K^{-1}	3249.0	[28]
Thermal conductivity of liquid	k_ℓ	W•m^{-1}•K^{-1}	0.468	[28]
Thermal conductivity of solid	k_s	W•m^{-1}•K^{-1}	2.7	[28]
Latent heat of fusion	Δh_f	J•kg^{-1}	3.18×10^5	[28]
Viscosity of liquid	μ_ℓ	kg•m^{-1}•s^{-1}	1.3×10^{-3}	[28]
Diffusion coefficient in liquid	D_ℓ	m^2•s^{-1}	4.8×10^{-9}	[28]
Boussinesq properties				
Liquid thermal expansion coefficient	β_T	K^{-1}	3.9×10^{-4}	[28]
Density difference	$\Delta\rho$	kg•m^{-3}	572.0	[1]
Liquid solutal expansion coefficient	β_C	wt.%$^{-1}$	2.87×10^{-3}	[28]
Other parameters				
Primary dendritic-arm spacing	λ_1	m	6.0×10^{-4}	[29]
Packing limit (grain envelope)	$f_{\text{e,packing}}$		0.637	[28]
Solid-to-envelope ratio in equiaxed	f_{si}		0.16	[30]
Constant in the fragmentation model	R		0.4	[8]

wall (left side of Fig. 3(b3) and (d3)) because the equiaxed crystals tend to accumulate less near the surface owing to the no-slip boundary condition. With time, the melt developed an anti-clockwise flow ($\vec{u}_\ell$ arrows in Fig. 3(b3)): grain sedimentation favored the central region of the domain (due to non-slip boundary condition) which forced the melt to move also downward in the center due to the coupling between the two phases (via the drag force); after the sedimentation of the grains, melt escaped the bottom region by flowing upward closer to the walls. Although the global solidification sequence was mostly unidirectional, the temperature field became clearly perturbed by the melt flow outside the columnar mushy zone (isolines in Fig. 3(e1)–(e3)).

At a later stage, as the upper part (columnar structure) and lower part (pile-up of the equiaxed fragments or columnar structure after the ECT event) approached each other, the melt convection weakened. Nevertheless, both the upper and lower parts of the solid structures continued to grow, and fragmentation events continued to occur at $t = 1000$s (Fig. 3(a4)–(e4)). Finally, the two opposing solid structures met at the center, thereby forming a microstructural transition. This was further discussed in the subsequent section.

3.2. Comparison between the simulation and experimental results

The temperature evolutions from the experimental and simulation results at six probe locations in test case 1 are shown in Fig. 4. The top surface was cooled; therefore, the temperature in probe 1 (P1) reduced sharply towards the specified temperature of the cold plate (i.e., 254.15 K). For the other probes (P2–P6), the temperature also decreased gradually with time. All the cooling curves show a good agreement between the experimental and simulation results. The only exception is the curve for P2 where the calculated temperature is higher than the experimental one. Note that no experimentally-determined cooling curves have been reported in [1] for test cases 2 to 5.

The evolution of the as-calculated solid structures is compared with the experimental results in [1] in Fig. 5(a)–(e). Results for the five test

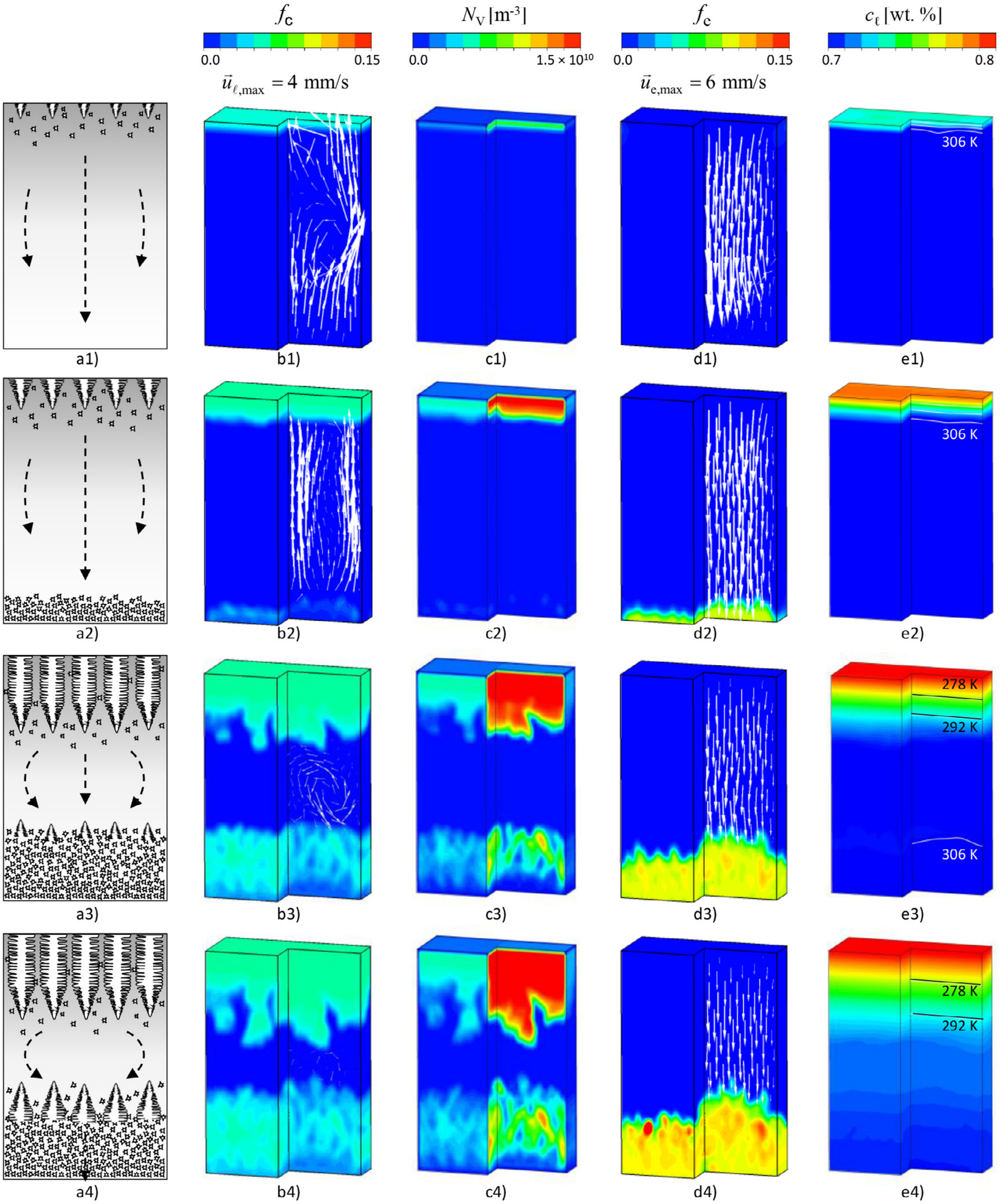

Fig. 3. Solidification sequence for test case 1 at (1) $t = 10$ s, (2) $t = 100$ s, (3) $t = 500$ s, and (4) $t = 1000$s (top to bottom). (a) Schematic representation of the main mechanisms, (b) f_c contour overlaid with $\vec{u}_\ell$ vectors, (c) N_v contour, (d) f_e contour overlaid with $\vec{u}_e$ vectors, and (e) c_ℓ contour overlaid with T isolines. The results are shown in 3D; however, a quarter of the domain is removed for the visualization of the internal fields.

cases (Table 2) were obtained. The curves represent the relative positions of the columnar-tip front coming from the top and pile-up of the equiaxed fragments (or the columnar-structure front growing from the packed equiaxed bed after ECT) at the bottom. The relative position was represented by the ratio of the location of the tip of the solid structure to the total height of the domain (i.e., dimensionless height). For reference, shadowgraphs at $t = 15$ s and $t = 120$ s for test case 1 are illustrated in Fig. 5(f) and (g), respectively.

The top surface was cooled to allow the columnar-dendritic structure to grow downward. This structure corresponds to the upper-black shadow from Fig. 5(f) and (g). The evolution of the columnar tip is shown in the top curve of each plot in Fig. 5(a)–(e). The columnar tip position starts with a dimensionless height of 1 and grows downward as the solidification progresses.

Meanwhile, equiaxed crystals originated from the fragmentation of the columnar dendrites. Because the fragments were heavier than the surrounding melt, they sedimented and piled up at the bottom of the test cell, as illustrated in Fig. 5(f) and (g). The dimensionless height of the bed of the fragments is presented in the bottom curve of each plot in Fig. 5(a)–(e). The height of the bed of fragments was observed to vary depending on the cooling conditions, alloy composition, and initial temperature of the melt.

In test case 1 (Fig. 5(a)), the agreement was quite good during the entire experiment and for both curves. After an initial high-fragmentation

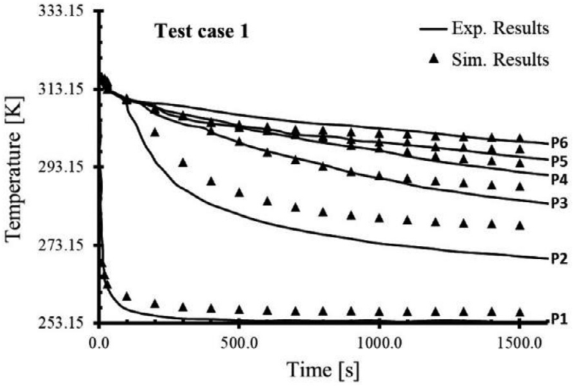

Fig. 4. Temperature evolution from the experimental and simulation results at six probe locations for test case 1.

rate, where the equiaxed bed piled up rapidly, the slope of the curve gradually flattened with time.

In test case 2 (Fig. 5(b)), the alloy composition changed from 68% (test case 1) to 66%. Although this meant that the fragmentation parameters (K_0, S_{s0}, and a) may be slightly different for this new alloy, the same fragmentation parameters were used owing to the lack of available data. The results showed that the fragmentation rate was higher than those of other test cases at the beginning of the experiment. This led to rapid sedimentation and piling up of fragments at the bottom of the test cell. The simulation captured this behavior, and the agreement between the experimental and simulation results was satisfactory. Although the magnitude of the piling up was slightly underestimated during the first stage of the simulation, the agreement improved with time. The two solid structures merged at the center of the domain later during the solidification process.

In test case 3 (Fig. 5(c)), the initial temperature of the melt was 4 K higher (the superheating temperature was 5 K) than that of test case 1. The profile of the bottom curve suggests that the growth evolution of the packed bed of the crystal fragments was more moderate than that of test case 1. Interestingly, in the simulations, the lower curve continued to rise with time because of the prevalent undercooling conditions existing in the domain at this point. This did not agree with the experimental results after approximately $t = 500$ s when the slope of the bottom curve became approximately flat. Before this point, and generally in the upper part of the solid structure, the agreement between the experimental data and the simulation results was good.

In test case 4 (Fig. 5(d)), the experimental conditions determined that the melt started at 13 K of superheating. Therefore, the fragments were subjected to a considerable amount of remelting that could lead to their disappearance when they passed through the largely superheated bulk melt. Although the remelting of the equiaxed crystals in the bulk-melt region was implemented here, replicating the experimental results was difficult for this test case. These results were discussed in detail in the subsequent section.

In test case 5 (Fig. 5(e)), similar to test case 1, the initial temperature of the melt increased by 4 K (the superheating temperature was 5 K) and the temperature of the cooling system was increased from 254.15 K to 259.15 K. The experimental and simulation results were in agreement during the gradual growth of the bottom and upper solid structures. This observation becomes particularly interesting given the fact that, in test case 3, which had stronger cooling conditions imposed on the top wall, the results indicated that the bottom solid-structure front stopped growing after a certain period.

3.3. Determination and validation of the fragmentation parameters

The parameters K_0, S_{s0}, and a must be determined to accurately replicate the capillary-driven fragmentation phenomenon. However, they have not yet been determined in the literature; therefore, here we attempted to estimate each of these parameters based on the experimental data provided in [1] (Fig. 5) and other currently available evidence in the literature. We assumed that the evolution of the bottom-crystal bed can indirectly reflect the equiaxed production rate via the fragmentation mechanism. Here, fragmentation was considered the only source of the equiaxed phase.

In the first attempt, K_0 was set at 23.5 $\mu m^3/s$ according to the K_0 for the Pb-Sn alloy [7]. A parametric study was then performed by

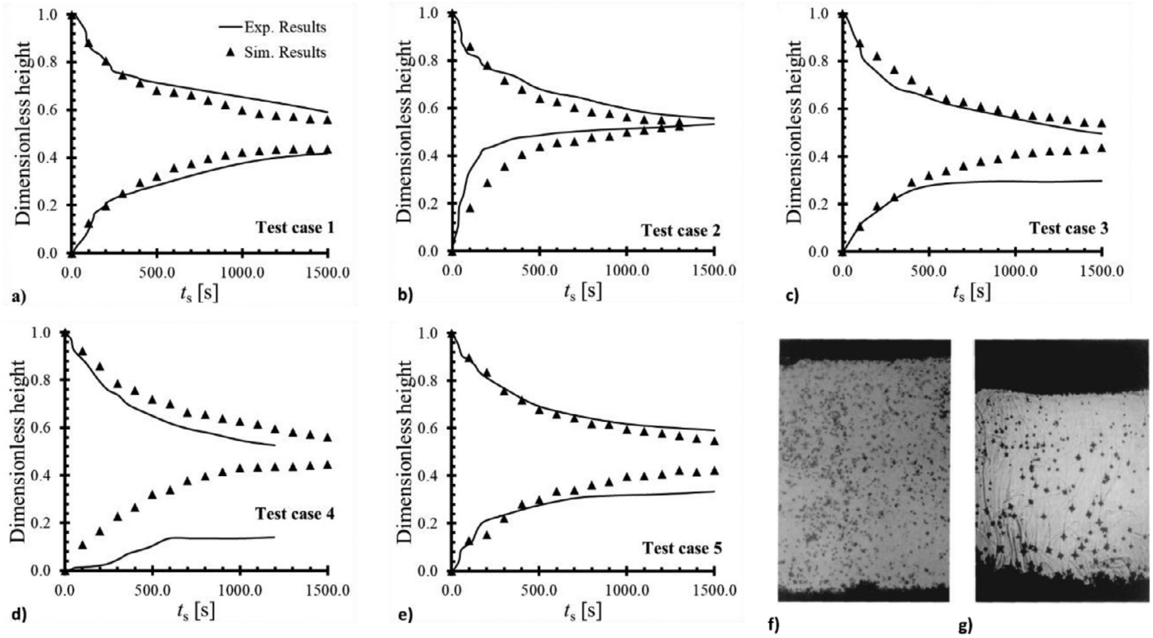

Fig. 5. Evolution of the dendritic-structure (columnar and equiaxed) fronts for all the five test cases (Table 2): (a) test case 1, (b) test case 2, (c) test case 3, (d) test case 4, and (e) test case 5. Shadowgraphs for test case 1 at (f) $t = 15$ s, and (g) $t = 120$ s (images replicated from [24] - Copyright © 1998 by The Minerals, Metals & Materials Society. Used with permission.).

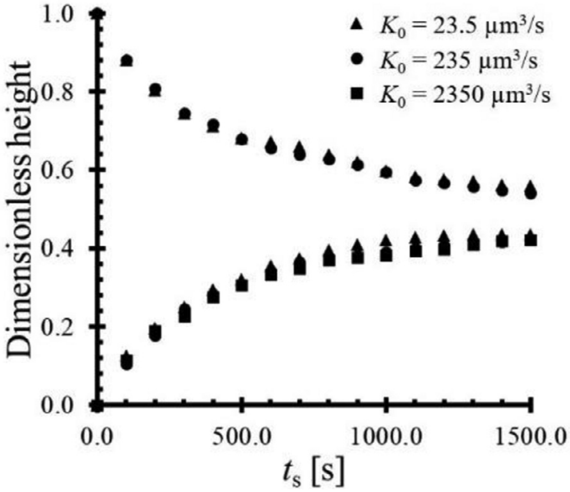

Fig. 6. Effect of K_0 on the evolution of the dendritic-structural (columnar and equiaxed) fronts. This parametric study was performed based on test case 1.

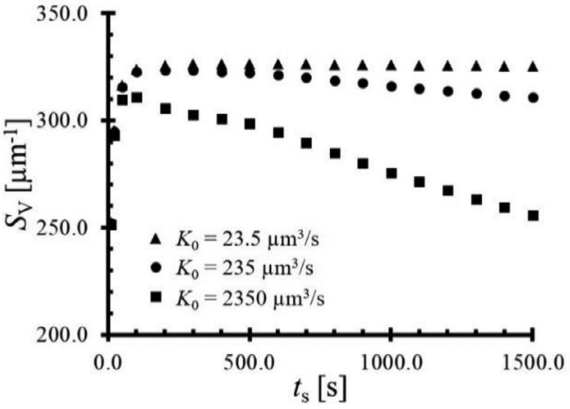

Fig. 7. Effect of K_0 on the $S_V - t_s$ curves for the top probe (P1). This parametric study was performed based on test case 1.

Table 4
Summary of the relevant simulation results obtained from the parametric study conducted with different values of $(S_{s0})^{-1}$.

$(S_{s0})^{-1}$ [μm]	d^0_{frag} [μm]	v_{set} [mm/s]	Pileup at $t = 15$ s
50	82	1.8	No
100	163	3.4	Yes
150	254	6.1	yes

increasing K_0 by one and two orders of magnitude. The evolution results of the columnar and equiaxed-structural fronts for test case 1 are shown in Fig. 6. Interestingly, the evolution of the structural fronts was not sensitive to K_0. This was because K_0 influenced the dendrite coarsening that occurred in the deep columnar-mushy zone (i.e., the late coarsening-dominant stage), whereas the evolution of the columnar and equiaxed-structure fronts depended mainly on the fragmentation events that occurred near the front of the columnar-mushy zone (i.e., the early solidification-dominant stage). The fragments created in the deep columnar-mushy zone during the coarsening-dominant stage could not be transported out of this zone, and they played no role in the evolution of the structural fronts.

Owing to its negligible impact on the evolution of the solid-structural fronts, K_0 was estimated by examining the evolution of S_V. In Fig. 7, the $S_V - t_s$ curves are plotted for the reference point (P1 probe) for test case 1. S_V increased sharply to a maximum value in the early solidification-dominant stage and gradually decreased during the coarsening-dominant stage. This decrease depended on K_0. For small values of K_0, S_V became nearly constant after reaching a peak value during the coarsening-dominant stage, thereby indicating that dendrite coarsening was almost negligible. For large values of K_0, the S_V profile started to develop a negative slope as the coarsening progressed: the larger the K_0, the steeper the slope and the larger the reduction in S_V with time (during the coarsening stage). Many studies have been conducted on the coarsening mechanism (e.g., [8,31–33]). In the present study, a K_0 of 2350 $\mu m^3/s$ was recommended for NH_4Cl-68 wt.% H_20 alloy because the corresponding $S_V - t_s$ curve shown in Fig. 7 revealed features similar to those of the general S_V evolution of dendrites reported by Neumann-Heyme et al. [8].

In contrast to K_0, S_{s0} influences the initial size of the fragments. A small value of S_{s0} results in a small S_V (Eq. (2)), thereby leading to a large initial fragment size (Eq. (5)). This relationship was used to assess the possible value of S_{s0} from the average fragment size at a particular instant by analyzing the shadowgraphs reported in [1] (Fig. 5(f) and (g)). For example, at $t = 15$ s, the estimated size of the fragments near the columnar-structure front ranged from 100 to 300 μm. The upper limit of 300 μm was directly measured from the sizes of the largest fragments observed in the shadowgraph in Fig. 5(f). The lower limit of 100 μm was derived from the settling velocity of the fragments. For an average fragment diameter smaller than 100 μm, the settling velocity was such that the fragments created at the columnar-tip front could not reach the bottom of the test cell in 15 s. In the shadowgraphs in [1], a bed of fragments was clearly observed at $t = 15$ s. A parametric study was then conducted to replicate test case 1 with different values of $(S_{s0})^{-1}$ that corresponded to the initial fragment sizes within the interval defined above. The results are summarized in Table 4.

At t = 15 s, an $(S_{s0})^{-1}$ of 100 μm resulted in an average fragment size of 163 μm at the top of the domain (i.e., close to the detachment event) and a settling velocity of 3.4 mm/s. Increasing $(S_{s0})^{-1}$ to 150 μm led to a fragment size of 254 μm and a settling velocity of 6.1 mm/s. This average fragment size was close to the maximum average-initial-fragment size suggested above. In this scenario, S_V was relatively small, which meant that the columnar structure was coarse and had only a few high-order arms. This was unlikely to occur because of the large fragmentation rate observed in the experiments. On the other hand, for an $(S_{s0})^{-1}$ of 50 μm, the average fragment size was 82 μm and the settling velocity was 1.8 mm/s. This initial fragment size was below the realistic range defined above, i.e., the settling velocity was too small to reach the bottom cell in 15 s and no pile-up was observed. Therefore, an $(S_{s0})^{-1}$ of 100 μm is recommended for this alloy.

To determine a (Eq. 3), a new parametric study was conducted by varying it from 1×10^{-4} (a of the Pb-Sn alloy [7]) to 200. Because a was used directly in Eq. (3), its effect can be directly observed on the number of fragments created from the columnar structure, which in turn affects the evolution of the tip front of the packed equiaxed structure. The results are shown in Fig. 8. Clearly, an a of 100 shows the best agreement with the experimental data. For a low value of a (e.g., $a = 50$), the fragmentation rate was low, and thus, too few created fragments sedimented and piled up at the bottom of the domain. This led to an underestimation of the bottom-solid structure. For an excessively large a (e.g., $a = 200$), the opposite scenario occurred. The present a is several orders of magnitude larger than that of the Pb-Sn alloy. This indicates that the fragmentation potential for a similar dendritic structure (i.e., with a similar S_V) is much larger for the NH_4Cl-H_20 alloy than for the Pb-Sn alloy.

In a previous study [19], we suggested that fragmentation should only occur once the solid fraction of the columnar phase had surpassed a specific threshold (f_{frag}) based on the assumption that the columnar structure had to be sufficiently developed before fragmentation can occur. A f_{frag} of 0.1 for an Al-Cu alloy was suggested. In the present study, owing to the extreme cooling conditions and strong fragmentation rate,

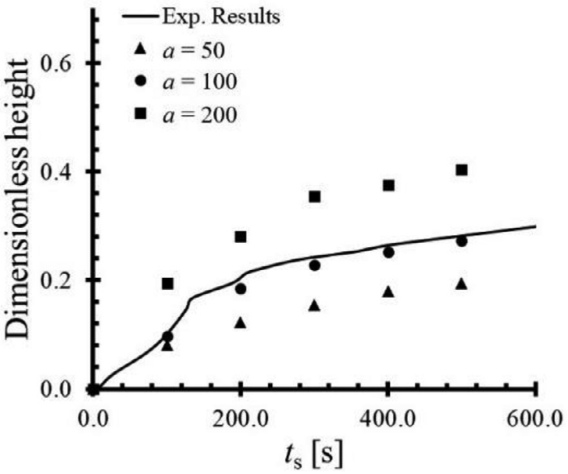

Fig. 8. Effect of *a* on the evolution of the tip front of the packed bed of crystal fragments. This parametric study was performed based on test case 1.

a f_{frag} of 0.1 was no longer appropriate. This value was also found to affect the evolution of the solid fraction of the primary-columnar structure. An excessively large f_{frag} can impede fragmentation, thereby leading to an overestimation of the local solid fraction of the columnar structure. The f_{frag} was set to 0.01 to avoid any effect of this parameter on the modeling outcome for the NH_4Cl-H_20 alloy.

4. Discussion

4.1. Temperature evolution

The temperature evolution governs the solidification kinetics; therefore, the simulation should be based on the correct thermal field, i.e., the calculated thermal fields should agree with the experimental ones. The thermal boundary conditions were not reported in [1]; however, the study provided cooling curves for test case 1 (Table 2). Therefore, the thermal boundary conditions were estimated by fitting the cooling curves obtained from the simulation to those obtained from the experiment. The comparison between the simulation results and experimental data for the temperature profiles are shown in Fig. 4. A very good agreement in almost all probe locations can be observed except for P2. The exact reason for this small discrepancy in P2 is not clear. However, this small discrepancy should not significantly affect the outcomes. In general, the comparison provided acceptable results despite the strong-cooling conditions in this experiment. Additionally, the uncertainty associated with the probe locations due to the scale resolution (which can significantly alter the curves), and with the approximations assumed in the cooling conditions at the top wall (constant and high HTC) and front and back surfaces (to replicate the heat transfer when the covers were removed for optical access) could explain the discrepancy in P2.

It should also be noted that only the cooling curves of test case 1 (Table 2) were provided in [1]. The thermal boundary conditions estimated based on the experiment in this test case were assumed to be valid for other test cases.

4.2. Remelting of the fragments

The current experimental configuration leads to very complex solidification phenomena, such as fragmentation, melt convection, grain transport, and the pile-up of equiaxed crystals [1]. As shown in Fig. 3, these phenomena can be reproduced by the numerical model. Additionally, several phenomena that were not discussed in detail in [1] were identified numerically: the potential growth of the columnar dendrites from the bed of equiaxed crystals (ECT), and the remelting of fragments in the bulk-melt region. According to Fig. 5, the experimentally-determined front positions of the solid structures from the upper and lower parts match the numerically calculated front positions. Among the five test cases, four showed good agreement between the simulations and experiments. In only one case (test case 4), the pile-up of crystal fragments was underestimated by the numerical model.

The main feature of test case 4 was that a high-melt superheat (13 K) was imposed as an initial condition. Consequently, in this experiment, the bed of fragments nearly disappeared in the first 200 s (Fig. 5(d)). This was in contrast with the simulation results where the bed of fragments, despite being smaller than those in the other test cases, was still clearly visible from the beginning (Fig. 5(d)). We assumed that this discrepancy was related to the remelting process that may not have been properly considered by the numerical model. This is discussed further below.

Fig. 9 shows the simulation results of the evolution of f_e and liquid-to-equiaxed mass transfer ($M_{\ell e}$) during the initial stage of solidification. The vectors represent the equiaxed velocity, and the black lines correspond to the columnar-tip front. At $t = 6$ s (Fig. 9(a)), a relatively large amount of f_e developed near the top of the domain where the columnar structure was growing downward: the fragmentation of the columnar dendrites had already occurred. Simultaneously, owing to the superheated melt, the fragments started to remelt, as confirmed by the negative $M_{\ell e}$ in this region in Fig. 9(a). Because the fragments were heavier than the melt, they began to sediment, as observed in Fig. 9(b) and (c) where the region with the equiaxed phase (f_e) appears progressively closer to the bottom surface. As they moved downward, the fragments continued to remelt ($M_{\ell e}$ was negative), and the local value of f_e and the region with fragments (gray area) reduced drastically. As shown in Fig. 9(d), a small bed of fragments appeared on the bottom surface. However, the absolute value of the solid fraction continued to be nearly negligible, and the $M_{\ell e}$ distribution indicated that the fragments continued to remelt. This description seems to agree with the experimental evidence shown in Fig. 5(d) where the dimensionless height of the fragmented structure is almost negligible during the first 200 s of the experiment.

However, as the simulation proceeded, the temperature gradually decreased and the superheat in the domain vanished owing to the strong cooling on the top surface. This is where the experimental and simulation results appeared to diverge at this point. The experimental results from Fig. 5(d) suggested that the bulk melt was probably superheated for almost 200 s. By contrast, in the simulation, the melt rapidly became undercooled, which indicated that the fragments began to solidify and grow while settling towards the bottom surface. This is demonstrated in Fig. 10(a), which shows the simulation results of the temperature evolution for test case 4 at the same probe positions as those defined in Fig. 2(b). After approximately 40 s, the temperatures of all the probes inside the domain were below the liquidus, which indicated that the fragments were expected to grow instead of remelt.

In Fig. 10(b), a detailed view of the simulation results of the evolution of the packed bed of equiaxed fragments in the first 100 s is presented. At $t = 10$ s, the height in the computational results is zero, which indicates that complete remelting of the fragments occurred, as suggested by Fig. 9(a)–(c). However, as the superheat gradually decreased, the remelting of the fragments became weaker and some fragments started to reach the bottom surface. At $t = 20$ s, a very small bed of fragments is observed, which supports the results shown in Fig. 9(d). Until $t = 50$ s, the total height was equal to the cell size used in the simulations. Notably, owing to the volume-average nature of the model, once the fragments sediments in a computational cell, the entire cell becomes nonzero. After $t = 50$ s, the undercooling conditions ensued (as confirmed by Fig. 10(a)), and the dimensionless height began to increase rapidly.

Even though the simulation results start with a good agreement with the experimental results during the first 50 s, after that, the pile-up of the packed bed of fragments was overestimated (Figs. 10(b) and 5(d)). No further information was provided in [1] for test case 4. However,

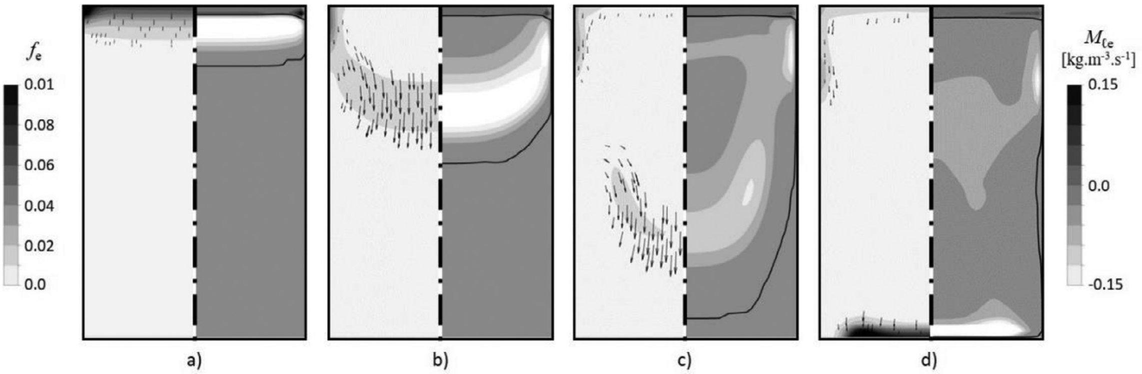

Fig. 9. Contours of f_e overlaid with $\vec{u}_e$ vectors (left) and $M_{\ell e}$ overlaid with the columnar-tip front (black line: right) at (a) $t = 6$ s, (b) $t = 10$ s, (c) $t = 14$ s, and (d) $t = 20$ s in test case 4. For $M_{\ell e}$, a positive value (dark gray) indicates solidification; a negative value (bright gray) indicates re-melting.

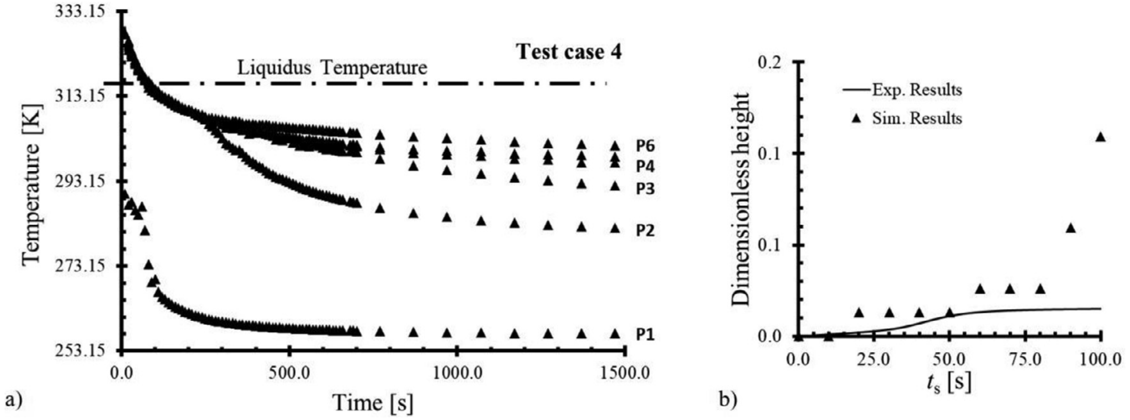

Fig. 10. (a) Detailed analysis of the cooling curves and (b) the evolution of the packed bed of equiaxed fragments, for test case 4.

the preparation of the experiment for a large superheat (13 K) could also explain this discrepancy. If the test cell was filled with a highly superheated melt for a long duration before commencing the experiment, the mold may begin to absorb some amount of heat. Thus, the adiabatic boundary conditions on the side and bottom walls assumed in the simulation would not be an accurate representation of the experimental case with a large superheat. We attempted a series of new simulations for test case 4 with heat flux boundary conditions applied to the walls (i.e., all the walls had the same constant heat flux value except for the cooled top surface). Although some improvements were achieved, the results continued to be unsatisfactory. Furthermore, for a sufficiently large heat flux that would ensure re-melting of the fragments before settling on the bottom surface, the superheated conditions propagated to higher parts of the domain and hindered the growth of the top columnar. Naturally, this could be improved with more accurate heat flux values or time-dependent functions; however, more information would be needed to perform such a study. Another possible source of error was the remelting model used in this study. However, owing to the lack of comprehensive understanding of the underlying physics of remelting, not much can be done here, apart from highlighting the need for further research on this topic.

Although the other test cases (1, 2, 3, and 5) began with some degree of superheating, the values were small and, combined with the intense cooling at the top surface, resulted in a rapid temperature decrease under the liquidus. As a result, most of the simulation time was spent under growth conditions that were well-described using the present model.

4.3. Microstructure evolution: CET vs. ECT

The crystal structure growing upward from the bottom surface stemmed from the pile-up of the fragments that were previously detached from the columnar dendrites on the top surface. After the initial fragmentation-heavy stage, the rate at which the fragments detached from the columnar dendrites gradually diminished with time. Meanwhile, a temperature gradient developed throughout the domain and the undercooled conditions reached the packed bed of fragments. Therefore, it is possible that, with the establishment of unidirectionally-oriented heat flux, the growth of the columnar structures may have been triggered in front of the packed crystal fragment bed.

Although no ECT has been mentioned in [1], this transition would be difficult to identify in the shadowgraphs. In contrast, our simulation model provides a complete time-dependent description of the microstructures. Fig. 11(a) shows the evolution of the bottom solid structure in test case 1 and identifies the leading morphology.

Once the local f_e^{env} in the packed bed of crystal fragments exceeds the packing limit ($f_{e,\text{packing}} = 0.637$), the equiaxed phase builds a rigid network that becomes stationary on encountering a stationary wall (such as the bottom surface). Numerically, this rigid and stationary equiaxed phase region is marked, and the primary-columnar dendrite is allowed to grow from the front of the marked region. At this point, the solidification of the columnar structure region competes with that of the equiaxed phase. The dominant phase is determined by the rate at which the primary-columnar dendrite grows in relation to the blocking capacity of the equiaxed phase. This means that the numerical model evaluates the volume fraction of the equiaxed phase (which can increase either because of the pile-up of new fragments or the solidification and growth of existing ones) and assesses the ability of the primary columnar-dendrite-tip front to move to neighboring cells before or after the f_e^{env} reaches the blocking limit $f_{e,\text{CET}}$ [34]. If the columnar-dendrite-tip front reaches a new cell while $f_e^{\text{env}} < f_{e,\text{CET}}$, the columnar structure becomes the dominant morphology and equiaxed growth is suppressed. However, fragments can still sediment and interact with (and poten-

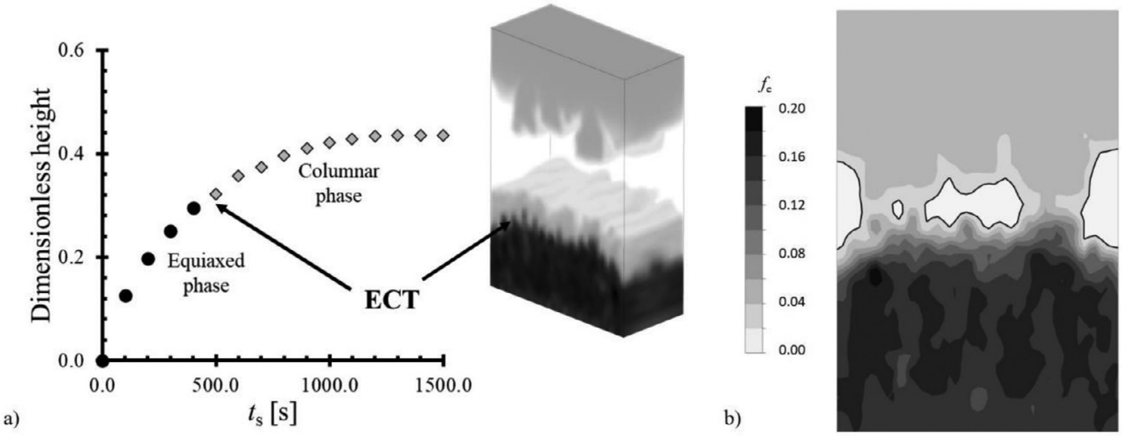

Fig. 11. (a) Evolution of the bottom solid structure in test case 1 and the specification of the dominant microstructure. (b) The volume fraction of the equiaxed phase when the bottom solid structure meets the top solid structure (t = 1300 s).

tially be captured by) the columnar structure. A blocking limit of 0.49 was originally suggested [35] but was later updated to 0.2 [36].

In test case 1, the rate at which the fragments detached from the columnar dendrite gradually diminished with time. This reduced the local-evolution rate of the packed bed of crystal fragments. From Fig. 11(a), at approximately t = 480 s, the primary columnar-dendrite-tip front grew to neighboring cells while $f_e^{env} < f_{e,CET}$. Therefore, the columnar morphology became dominant, and an ECT event occurred, i.e., solidification continued as a columnar structure, and the equiaxed growth was suppressed. The final ECT position was identified in Fig. 11(a). The microstructure transition is also visible in the inset of Fig. 11(a) where the equiaxed-dominant morphology is displayed in black and the columnar-dominant morphology is displayed in gray.

Subsequently, during the casting process, the new columnar structure growing from the bottom met the one growing from the top. This is suggested in Fig. 5(b) and is now illustrated in Fig. 11(b) for test case 2 at t = 1300s.

4.4. Validity of the flow-driven fragmentation

We previously presented a flow-driven fragmentation model [17,34]. The formulation assumed that the transport of the solute-enriched melt through the interdendritic flow in the columnar-growth direction led to remelting and was the main cause of fragmentation [18,37]. Consequently, the melt flowing parallel to the columnar-growth direction was a necessary condition to trigger fragmentation, and the fragmentation rate was calculated as follows:

$$\dot{N}_V = \frac{M_{ce}}{\rho_e V_e} = \frac{-\gamma\left(\vec{u}_\ell - \vec{u}_c\right)\cdot\nabla c_\ell\,\rho_e}{\rho_e \frac{\pi}{6}\left(d^0_{frag}\right)^3} \tag{6}$$

where $\vec{u}_\ell$ and $\vec{u}_c$ correspond to the liquid and columnar velocities, respectively, and γ is a fitting coefficient that includes all the unknown contributing factors not considered by the model, such as the curvature effect of the dendrites, latent heat-induced thermal fluctuation, and solute diffusion in the interdendritic melt. γ was estimated in [17] by curve-fitting the experimental results. d^0_{frag} in Eq. (6) for the flow-driven fragmentation model was calculated as $f_c\lambda_2$ [17] (instead of Eq. (5) used in the capillary-driven fragmentation model), with λ_2 being the secondary dendrite arm spacing and equal to 1.0×10^{-4} m. The concentration gradient, ∇c_ℓ, in the interdendritic melt typically increases against the columnar growth direction. Therefore, from Eq. (6), the interdendritic melt flowing in the same direction as the columnar growth results in $-(\vec{u}_\ell - \vec{u}_c)\cdot\nabla c_\ell > 0$. This promotes remelting that results in fragmentation. This model was termed the flow-driven fragmentation model, which is different from the capillary-driven fragmentation model used in this study.

In Fig. 12, the experimental results of the evolution of the structural fronts in test case 1 are compared with the simulation results that employed the flow-driven fragmentation model. No data are available for γ for the current alloy; therefore, a parametric study was conducted by varying this parameter. The simulation results for the coarsening-driven fragmentation model are not shown in this figure to avoid overcrowding; however, they can be observed in Fig. 5(a). For $\gamma = 1$, the underestimated bed of fragments and excessive columnar growth suggested that the fragmentation rate was too low. On increasing γ by one order of magnitude (i.e., $\gamma = 10$), the fragmentation rate increased such that the evolution of the bed of fragments surpassed that measured experimentally. However, columnar growth was also overestimated, which can be a sign that insufficient fragments detached from the columnar structure. On increasing γ by another order of magnitude (i.e., $\gamma = 100$), good agreement between the experimental and numerical results was obtained for the columnar evolution from the top surface. However, the growth of the fragment bed was greatly overestimated.

These results indicate that the flow-driven fragmentation model cannot appropriately account for the fragmentation mechanism observed in the experiments reported in [1]. However, we also applied both fragmentation models to different solidification conditions for a metal alloy (Al-7 wt.% Si). The conditions involved unidirectional solidification under forced flow conditions (strong rotational magnetic stirring). Interestingly, in this study, the experimental results were in better agreement with the flow-driven fragmentation model than with the coarsening-driven fragmentation model. This on-going study will be published in the future.

This difficulty in finding a general formulation to accurately replicate the fragmentation process can indicate that different mechanisms may be involved depending on the conditions of the experiment. For instance, the dendrite morphology can change considerably with different alloys. In ammonium chloride, f_{si} (0.16) (see Table 3) is generally much smaller than those for metal alloys (e.g., in Pb-Sn alloys f_{si} = 0.5 [34] and Al-Cu alloys f_{si} = 0.5 [17]). This indicates that the dendritic structure is more fragile in ammonium chloride than in metal alloys. Similarly, the S_V values for the dendrites of ammonium chloride seem to be much larger than those of metal alloys. In the present study, S_V surpassed 300 μm^{-1} (see Fig. 7), whereas S_V only reached 0.1 μm^{-1} under intense cooling in our previous study on the fragmentation in a Pb-Sn alloy [19]. Although the setup and cooling conditions were distinct in the two examples, they should not account for the difference of several orders of magnitude. Both of the above observations imply that ammonium chloride dendrites have thin high-order arms that can

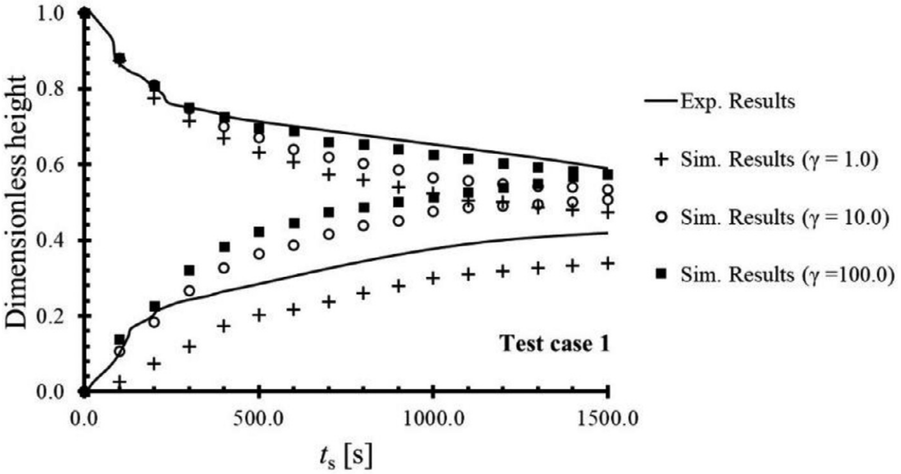

Fig. 12. Evolution of the solid dendrite-structure fronts in test case 1 from the experimental and simulation results using the flow-driven fragmentation model with different γ values.

be easily remelted via coarsening. This is also supported by the values proposed for a in the coarsening-driven model; for ammonium chloride, we proposed an a of 100, whereas Cool and Voorhees [7] proposed an a of 0.5×10^{-4} for a Pb-Sn alloy. A large a for ammonium chloride implies a high fragmentation rate from coarsening. This can explain the validation of the coarsening-driven fragmentation model in the present study through experiments involving ammonium chloride.

In contrast, for metal alloys, thick high-order arms weaken the role of coarsening-driven fragmentation and strengthen the role of melt flow-driven fragmentation. Although Cool and Voorhees [7] still observed fragments in a Pb-Sn alloy originating from coarsening, the experiments were conducted under microgravity conditions (i.e., a complete absence of flow), the total number of fragments was smaller, and a larger timeframe was considered than in the experiments conducted in [1]. Therefore, in general, if a strong flow (forced flow condition) is considered for metal alloys, the flow-driven fragmentation mechanism seems to be more important than the coarsening-driven fragmentation mechanism. Further experimental studies are needed to analyze ammonium chloride and metal alloys under forced flow conditions and different levels of cooling to validate the above statement.

5. Conclusions

A capillary-driven fragmentation model was implemented in a volume-average mixed columnar-equiaxed solidification model and validated against a solidification experiment with NH_4Cl-68 wt.% H_20 alloy. In the experiment, crystal fragmentation and multiphase transport phenomena, such as melt convection and grain transport, were observed to play a critical role in the outcome. Five experimental cases with variations in the initial nominal composition of the alloy, initial melt temperature, and cooling intensity were analyzed.

Numerical parametric studies and experimental data analyzes were combined to determine the alloy-dependent constants that were essential to the fragmentation model. For the NH_4Cl-68 wt.% H_20 alloy, the following parameters were suggested: $(S_{s0})^{-1} = 100$ μm and $a = 100$. The parameter K_0 was approximated as 2350 $\mu m^3/s$ according to the profile of the coarsening-dominant stage and by taking the $S_V - t_s$ curves proposed by Neumann-Heyme et al. [8] as a reference.

The comparison of the structural evolution between the simulation results and experimental data provided an excellent quantitative agreement in four of the five experimental cases. This agreement proved the reliability of the capillary-induced fragmentation model and its implementation in the mixed columnar-equiaxed solidification model. The reason for the quantitative mismatch in one of the experimental cases, where high-initial superheating (13 K) was considered, was also discussed. In this case, the evolution speed of the bottom pile-up of equiaxed crystals was overestimated by the numerical simulation. During the early stage of the process, the fragments that were transported through the superheated bulk-melt region were remelted. Although the current solidification model considered the remelting phenomenon, the remelting rate was not calculated precisely. The remelting part of the model may require further improvement.

Another interesting phenomenon, i.e., ECT, was predicted by the simulations. This was not mentioned in [1]. During the late stage of solidification, the number of fragments decreased and the pile-up of the bottom crystal fragments (i.e., equiaxed crystals) slowed down. Owing to the undercooled-bulk melt, a columnar structure developed and grew upward, thereby leading to ECT. Finally, this columnar structure (after the ECT event) growing from the bottom met that growing from the top.

For comparison, a flow-driven fragmentation formulation that was previously proposed and used by the authors for other metal alloys such as Sn-10 wt.% Pb [17], has been considered in the solidification model in lieu of the coarsening-driven fragmentation formulation. However, there was no proper agreement between the results obtained from the flow-driven fragmentation model and the experimental results in this study (NH_4Cl-68 wt.% H_20). This emphasized that the coarsening-driven fragmentation model provided a good description of the fragmentation phenomenon observed in this study with NH_4Cl-68 wt.% H_20 alloy [1].

Declaration of Competing Interest

The authors declare that they have no known competing financial interests or personal relationships that could have appeared to influence the work reported in this paper.

Acknowledgment

This study was supported by the FWF Austrian Science Fund in the framework of the FWF-NKFIN joint project (FWF, I4278-N36).

References

[1] J.W. Gao, C.Y. Wang, An Experimental Investigation Into the Effects of Grain Transport on Columnar to Equiaxed Transition During Dendritic Alloy Solidification, J. Heat Transf. 121 (1999) 430–437.
[2] M.C. Flemings, Coarsening in Solidification Processing, Mater. Trans. 46 (2005) 895–900.
[3] A. Hellawell, S. Liu, S.Z. Lu, Dendrite fragmentation and the effects of fluid flow in castings, JOM 49 (1997) 18–20.
[4] D.M. Herlach, K. Eckler, A. Karma, M. Schwarz, Grain refinement through fragmentation of dendrites in undercooled melts, Mater. Sci. Eng. A 304–306 (2001) 20–25.
[5] L.K. Aagesen, A.E. Johnson, J.L. Fife, P.W. Voorhees, M.J. Miksis, S.O. Poulsen, E.M. Lauridsen, F. Marone, M. Stampanoni, Pinch-off of rods by bulk diffusion, Acta Mater. 59 (2011) 4922–4932.

[6] H. Yasuda, K. Morishita, N. Nakatsuka, T. Nishimura, M. Yoshiya, A. Sugiyama, K. Uesugi, A. Takeuchi, Dendrite fragmentation induced by massive-like δ–γ transformation in Fe–C alloys, Nat. Commun. 10 (2019) 3183.

[7] T. Cool, P.W. Voorhees, The evolution of dendrites during coarsening: Fragmentation and morphology, Acta Mater. 127 (2017) 359–367.

[8] H. Neumann-Heyme, K. Eckert, C. Beckermann, General evolution equation for the specific interface area of dendrites during alloy solidification, Acta Mater. 140 (2017) 87–96.

[9] J. Pilling, A. Hellawell, Mechanical deformation of dendrites by fluid flow, Metall. Mater. Trans. A 27a (1996) 229–232.

[10] R.H. Mathiesen, L. Arnberg, P. Bleuet, A. Somogyi, Crystal fragmentation and columnar-to-equiaxed transitions in Al-Cu studied by synchrotron X-ray video microscopy, Metall. Mater. Trans. A 37 (2006) 2515–2524.

[11] E. Liotti, A. Lui, S. Kumar, Z. Guo, C. Bi, T. Connolley, P.S. Grant, The spatial and temporal distribution of dendrite fragmentation in solidifying Al-Cu alloys under different conditions, Acta Mater. 121 (2016) 384–395.

[12] D. Ruvalcaba, R.H. Mathiesen, D.G. Eskin, L. Arnberg, L. Katgerman, In situ observations of dendritic fragmentation due to local solute-enrichment during directional solidification of an aluminum alloy, Acta Mater. 55 (2007) 4287–4292.

[13] Q. Han, A. Hellawell, Primary particle melting rates and equiaxed grain nucleation, Metall. Mater. Trans. B 28 (1997) 169–173.

[14] H. Neumann-Heyme, K. Eckert, C. Beckermann, Dendrite fragmentation in alloy solidification due to sidearm pinch-off, Phys. Rev. E Stat. Nonlinear Soft Matter Phys. 92 (2015) 1–5.

[15] E. Wesner, A. Choudhury, A. August, M. Berghoff, B. Nestler, A phase-field study of large-scale dendrite fragmentation in Al–Cu, J. Cryst. Growth 359 (2012) 107–121.

[16] Q. Zhang, H. Fang, H. Xue, S. Pan, M. Rettenmayr, M. Zhu, Interaction of local solidification and remelting during dendrite coarsening - modeling and comparison with experiments, Sci. Rep. 7 (2017) 1–13.

[17] Y. Zheng, M. Wu, A. Kharicha, A. Ludwig, Incorporation of fragmentation into a volume average solidification model, Modell. Simul. Mater. Sci. Eng. 26 (2018) 1–18.

[18] M.C. Flemings, G.E. Nereo, Macrosegregation: Part 1, Trans. Soc. Aime 239 (1967) 1449–1461.

[19] C.M.G. Rodrigues, M. Wu, H. Zhang, A. Ludwig, A. Kharicha, Bridging Capillary–Driven Fragmentation and Grain Transport with Mixed Columnar-Equiaxed Solidification, Metall. Mater. Trans. A 52 (2021) 4609–4622.

[20] M. Wu, A. Ludwig, A three-phase model for mixed columnar-equiaxed solidification, Metall. Mater. Trans. A 37 (2006) 1613–1631.

[21] M. Wu, A. Ludwig, A. Kharicha, Volume-Averaged Modeling of Multiphase Flow Phenomena during Alloy Solidification, Metals 9 (2019) 229 (Basel).

[22] J. Lipton, M.E. Glicksman, W. Kurz, Dendritic growth into undercooled alloy metals, Mater. Sci. Eng. 65 (1984) 57–63.

[23] H. Zhang, M. Wu, P. Schumacher, C.M.G. Rodrigues, A. Ludwig, A. Kharicha, Modelling melting and grain destruction phenomena during globular equiaxed solidification, Appl. Math. Modell. 97 (2021) 821–838.

[24] B. Thomas, C. Beckermann, Modeling of casting, welding, and Advanced Solidification Processes VIII, Minerals, 8th ed., Metals & Materials Society, 1998.

[25] M. Stefan-Kharicha, A. Kharicha, J. Mogeritsch, M. Wu, A. Ludwig, Review of Ammonium Chloride–Water Solution Properties, J. Chem. Eng. Data 63 (2018) 3170–3183.

[26] A. Ramani, C. Beckermann, Dendrite tip growth velocities of settling NH4Cl equiaxed crystals, Scr. Mater. 36 (1997) 633–638.

[27] R. Perry, D. Green, J. Maloney, Perry's Chem. Engineers' Handbook, 7th ed., McGraw-Hill, 1999.

[28] C.Y. Wang, C. Beckermann, Equiaxed dendritic solidification with convection: Part I. Multiscale/multiphase modeling, Metall. Mater. Trans. A 27 (1996) 2754–2764.

[29] M. Stefan-Kharicha, A. Kharicha, M. Wu, A. Ludwig, Observation of flow regimes and transitions during a columnar solidification experiment, Fluid Dyn. Res. 46 (2014) 1–21.

[30] M. Wu, M. Stefan-Kharicha, A. Kharicha, A. Ludwig, Hydrodynamically enhanced electrochemical mass transferon the surface of an electrically conductive dropet, Int. J. Heat Mass Transf. 164 (2021) 120566.

[31] S.P. Marsh, M.E. Glicksman, Overview of Geometric Effects on Coarsening of Mushy Zones, Metall. Mater. Trans. A 27 (1996) 557–567.

[32] H. Neumann-Heyme, N. Shevchenko, Z. Lei, K. Eckert, O. Keplinger, J. Grenzer, C. Beckermann, S. Eckert, Coarsening evolution of dendritic sidearms: From synchrotron experiments to quantitative modeling, Acta Mater. 146 (2018) 176–186.

[33] H. Zhang, M. Wu, C.M.G. Rodrigues, A. Ludwig, A. Kharicha, Directional Solidification of AlSi7Fe1 Alloy Under Forced Flow Conditions: Effect of Intermetallic Phase Precipitation and Dendrite Coarsening, Metall. Mater. Trans. A 52 (2021) 3007–3022.

[34] Y. Zheng, M. Wu, A. Kharicha, A. Ludwig, Numerical analysis of macrosegregation in vertically solidified Pb-Sn test castings—Part II: Equiaxed solidification, Comput. Mater. Sci. 124 (2016) 456–470.

[35] J.D. Hunt, Steady state columnar and equiaxed growth of dendrites and eutectic, Mater. Sci. Eng. 65 (1984) 75–83.

[36] V. Biscuola, M. Martorano, Mechanical Blocking Mechanism for the Columnar to Equiaxed Transition, Metall. Mater. Trans. A 39 (2008) 2885–2895.

[37] T. Campanella, C. Charbon, M. Rappaz, Grain refinement induced by electromagnetic stirring: A dendrite fragmentation criterion, Metall. Mater. Trans. A 35 (2004) 3201–3210.